4D rotational x-ray imaging of wrist joint dynamic motion

Carelsen, B.; Bakker, N.H.; Strackee, S.D.; Boon, S.N.; Maas, M.; Sabczynski, J.; Grimbergen, C.A.; Streekstra, G.J.

DOI
10.1118/1.2000647

Publication date
2005

Published in
Medical Physics

4D rotational x-ray imaging of wrist joint dynamic motion

Bart Carelsen[a)] and Niels H. Bakker
Department of Medical Physics, Academic Medical Center, PO Box 22660, 1100 DD Amsterdam, The Netherlands

Simon D. Strackee
Department of Plastic and Reconstructive Surgery, Academic Medical Center, PO Box 22660, 1100 DD Amsterdam, The Netherlands

Sjirk N. Boon
Department of Clinical Science and Applications, GXR Surgery, Philips Medical Systems, PO Box 10000, 5680 DA, Best, The Netherlands

Mario Maas
Department of Radiology, Academic Medical Center, PO Box 22660, 1100 DD Amsterdam, The Netherlands

Jörg Sabczynski
Philips Research Laboratories, Division Technical Systems, Roentgenstrasse 24-26, D-22335 Hamburg, Germany

Cornelis A. Grimbergen and Geert J. Streekstra
Department of Medical Physics, Academic Medical Center, PO Box 22660, 1100 DD Amsterdam, The Netherlands

(Received 17 November 2004; revised 20 June 2005; accepted for publication 20 June 2005; published 22 August 2005)

Current methods for imaging joint motion are limited to either two-dimensional (2D) video fluoroscopy, or to animated motions from a series of static three-dimensional (3D) images. 3D movement patterns can be detected from biplane fluoroscopy images matched with computed tomography images. This involves several x-ray modalities and sophisticated 2D to 3D matching for the complex wrist joint. We present a method for the acquisition of dynamic 3D images of a moving joint. In our method a 3D-rotational x-ray (3D-RX) system is used to image a cyclically moving joint. The cyclic motion is synchronized to the x-ray acquisition to yield multiple sets of projection images, which are reconstructed to a series of time resolved 3D images, i.e., four-dimensional rotational x ray (4D-RX). To investigate the obtained image quality parameters the full width at half maximum (FWHM) of the point spread function (PSF) via the edge spread function and the contrast to noise ratio between air and phantom were determined on reconstructions of a bullet and rod phantom, using 4D-RX as well as stationary 3D-RX images. The CNR in volume reconstructions based on 251 projection images in the static situation and on 41 and 34 projection images of a moving phantom were 6.9, 3.0, and 2.9, respectively. The average FWHM of the PSF of these same images was, respectively, 1.1, 1.7, and 2.2 mm orthogonal to the motion and parallel to direction of motion 0.6, 0.7, and 1.0 mm. The main deterioration of 4D-RX images compared to 3D-RX images is due to the low number of projection images used and not to the motion of the object. Using 41 projection images seems the best setting for the current system. Experiments on a postmortem wrist show the feasibility of the method for imaging 3D dynamic joint motion. We expect that 4D-RX will pave the way to improved assessment of joint disorders by detection of 3D dynamic motion patterns in joints.
[DOI: 10.1118/1.2000647]

I. INTRODUCTION

To evaluate wrist functioning the analysis of three-dimensional (3D) patterns of movement of the carpal bones in the wrist joint is crucial. *In vitro* 3D animations and models of the complex joint motion have been deduced from the motion of extremities[1–3] using external reference frames, which are not applicable in *in vivo* studies. A review of literature on *in vivo* carpal analysis on carpal bones image can be found in Mooijen *et al.*[4] State of the art 3D imaging methods allow only a static display of carpal bones.[5,6] Repeated imaging of 3D carpal bones at multiple static poses of the hand provides only an animated movement pattern. However, a dynamic movement pattern of carpal bones may deviate from its animated counterpart due to neuromuscular control and dynamic properties of ligaments and cartilage in the wrist. From two-dimensional (2D) video radiographic observations we know that clinically significant abrupt changes in orientation and position of carpal bones can occur during dynamic movement.[7] These abrupt changes do not occur during static poses in the absence of wrist movement used for animated imaging. *In vivo* dynamic measurements of 3D movement patterns have been performed with 2D (bi-

plane) fluoroscopy[8,9] registration to 3D computed tomography (CT) images, however, only applied to the knee, which is less complex to match since there are only two bones. Biplane dynamic 3D imaging of the more complex wrist requires several x-ray modalities and sophisticated matching algorithms.

In this article a method for 3D dynamic imaging of the wrist is introduced, which uses a modified mobile C-arm system with 3-D rotational x-ray (3D-RX) capabilities. This 3D-RX system allows acquisition of a number of x-ray projection images along a semicircular arc, which are reconstructed to a 3D data set[10] similar to CT. The open geometry of the C-arm provides a compliant workspace for several postures. For four-dimensional rotational x ray (4D-RX) we propose using the 3D-RX system to make a series of time resolved volume reconstructions of an object that is forced into a cyclic motion. This approach is closely related to the image acquisition method applied in ECG-gated 3D-rotational coronary angiography,[11] ECG gated coronary angiography with multislice computed tomography,[12,13] or respiratory gated cone-beam CT.[14,15] Instead of the retrospective gating used in these methods, we apply prospective synchronization of the image acquisition with the cyclic motion of the wrist. This procedure yields a number of volume reconstructions of the wrist at different phases of its cyclic motion.

To investigate the feasibility of 4D-RX we performed tests with a phantom to obtain image quality as a function of imaging parameters. In addition the image quality of our setup is illustrated by imaging a postmortem wrist.

II. IMAGING OF DYNAMIC MOTION PATTERNS

In its conventional application for imaging of static objects a mobile C-arm 3D-RX system[16] acquires a number of x-ray projection images from different angles. This is done with a prototype BV Pulsera (Philips Medical Systems, Best NL) mobile C-arm system. The C-arm is motorized to make a propeller movement over a semicircular track at constant speed meanwhile acquiring projection images. For adequate 3D-RX reconstruction, an angle of 180 degrees+cone angle is covered. The dose is automatically adjusted during the run to obtain optimal images from the image intensifier TV system. The pulsed images, acquired at constant acquisition frequency, are sent to a modified 3-dimensional-rotational angiography (3D-RA) workstation.[10] The image geometry of the projection is calibrated beforehand and is used in the reconstruction. The projection images, corrected for image and geometry distortions, are then reconstructed to a 3D dataset, which is a 3D-RX reconstruction representing a tomographic x-ray image. The reconstruction is done with a modified Feldkamp filtered backprojection algorithm.[17] The dose automation, voxel scaling, and beam geometry (not all what is irradiated is also reconstructed) provide that there is no absolute radio density scale like the Hounsfield scale in CT but this does not affect the image quality measurements.

When the object is moving, a 3D image at a certain phase in the motion cycle can be obtained if all projection images within a set used for reconstruction are acquired at the moment that the object passes the same point in the motion cycle. When multiple sets of projection images are acquired during a movement cycle, multiple 3D-RX reconstructions of the moving object at different motion phases are obtained, together forming the 4D-RX image.

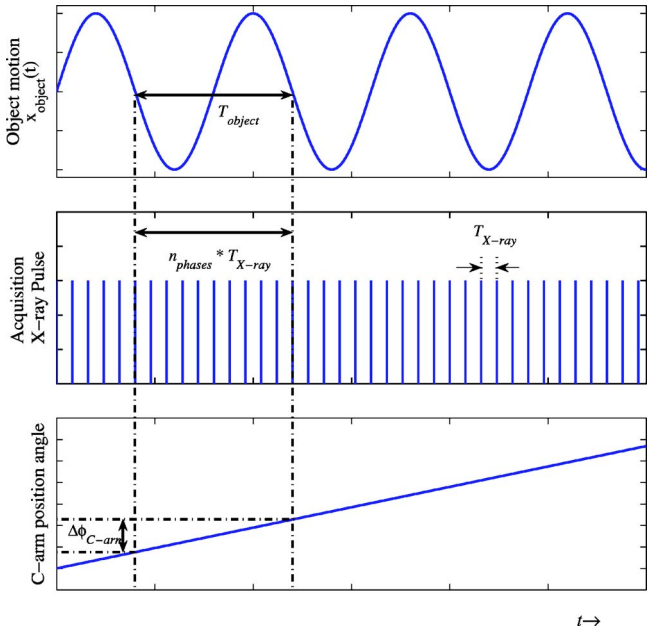

FIG. 1. A time fragment of the 4D-RX acquisition. The C-arm is rotated around the cyclic moving object (with period T_{object}). Meanwhile projection images are acquired with a period of $T_{x\ \text{ray}}$. Projection images from identical phase of the object motion are acquired on regular time intervals $n_{\text{phases}}{}^{*}T_{x\ \text{ray}}$ corresponding to C-arm rotation angle intervals $\Delta\phi_{C\text{-arm}}$.

For 4D-RX, a mobile C-arm is rotated around a cyclic moving object that has frequency f_{object} or period $T_{\text{object}}=f_{\text{object}}^{-1}$. During rotation of the C-arm, x-ray projection images are acquired of the moving object that is located in the center of rotation. The acquisition of projection images is performed at a fixed frequency $f_{x\ \text{ray}}$ or period $T_{x\ \text{ray}}=f_{x\ \text{ray}}^{-1}$ (see Fig. 1).

To ensure multiple projection images at the same phase of the motion, the frequency of the cyclic object motion f_{object} and the acquisition frequency $f_{x\ \text{ray}}$ of the x-ray system must be synchronized and follow the relationship

$$f_{\text{x ray}} = n_{\text{phases}} \cdot f_{\text{object}}, \tag{1}$$

where n_{phases} is the integer number of phases of the object motion cycle that are imaged. The projection images belonging to the same phase of object motion are grouped. For each phase an equal number of projection images are obtained

$$n_{\text{projections}} = \frac{f_{\text{x ray}} \cdot D_{\text{x ray}}}{n_{\text{phases}}} = \frac{\phi_{\text{C-arm,total}}}{\Delta\phi_{\text{C-arm}}}, \tag{2}$$

with $D_{x\ \text{ray}}$ the total duration of the 3D-RX scan, $\phi_{C\text{-arm,total}}$ the total C-arm rotation, and $\Delta\phi_{C\text{-arm}}$ the C-arm rotation in one object motion cycle (Fig. 1). Each element in the set of n_{phases} reconstructions has its own phase in the motion cycle

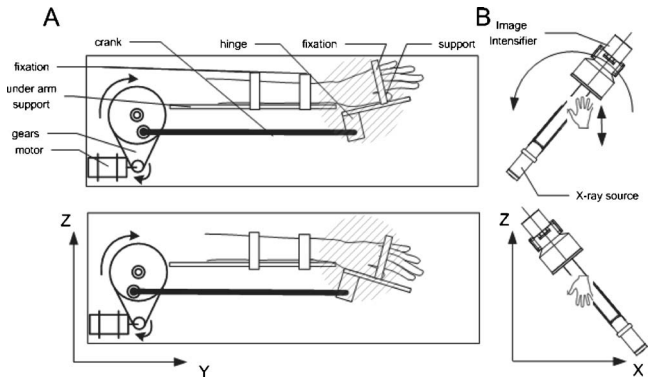

FIG. 2. Schematic drawing of the movement device in two positions from a side (a) and front (b) view. In part (a) the *YZ* plane the motor and gears are shown, on the right the crank driving the upward-downward movement of the hand x_{object}. This part is situated in the volume of reconstruction (the shaded circle) and is therefore wrapped in low density plastic. In part (b) the *XZ* plane with the C-arm's detector rotating from the positive to the negative *X* axis over the positive *Z* axis while the object moves up and down along the *Z* axis.

and together the reconstructions form a dynamic 3D image, i.e., a 4D-RX image.

III. EQUIPMENT

For the image acquisition, a BV Pulsera 3D-RX prototype is used. The system is modified to perform a motorized rotation over 200 degrees starting and ending in approximate horizontal position (*x* axis, see Fig. 2). The system is able to take pulsed fluoroscopic images with pulse length between 8 and 13 ms and with acquisition frequencies $(f_{x\ \text{ray}})_{\text{in}}$ the range 1–25 Hz, with a maximum of 375 images or maximal 30 s scan duration. The x-ray pulses have an amplitude of 60 mA and automated voltage control. In the case of a wrist, the voltage stabilizes around 50 kV, resulting in an effective dose of only 0.1 mSv. The projection images are sent to a modified 3D-RA release 3.2 workstation for reconstruction (Philips Medical Systems, Best, The Netherlands). Beforehand the system is calibrated in two steps as described in Koppe *et al.*[18,19] First, the pincushion distortion of the image intensifier, S-distortion due to the magnetic field and focal spot are calibrated; second, the C-arm geometry is calibrated. The workstation reconstructs a 3D data set from all projection images in a spherical field of view with a diameter of 18 cm. The 3D-RX reconstruction is a volume image of $256\times256\times256$ voxels, which are isotropic with a size of 0.7 mm.

The point spread function (PSF) is not isotropic partly due to radial undersampling. In the case of a semicircular arc +cone beam, parker weighting has to be applied.[20] This procedure with a rotation around the *Y* axis (propeller rotation of the C-arm, see Fig. 2) yields the best spatial resolution in the horizontal plane (*XY* plane, Fig. 2), similar like Wu *et al.*[21] However, the Parker weighting absence in our reconstruction causes an additional blur on the *X* axis. This results the PSF to be at best in the *Z* direction. This is parallel to the direction of motion of the object and allows optimal investigation of possible motion blur.

A movement device has been developed to impose a cyclic motion to an object. A direct current (DC) motor drives a mechanical transmission to move the object 40 degrees up and down (Fig. 2). The entire movement lies within the volume of reconstruction. The dc motor with speed reduction is feedback controlled to ensure a constant frequency of motion. The cycle of the object is tracked with an electronic sensor to enable synchronization with the 3D-RX system. Object movement and x-ray signal are displayed on a digital oscilloscope and verified. After manual synchronization, the acquisition of the projection images is started. Next, the projection images are sorted and reconstructed as described in the previous section.

IV. EXPERIMENTS

Deviations in the object movement result an unmistakable failure of 3D-RX reconstruction containing apparent motion artifacts. If the synchronization conditions are not obeyed the x ray and motion will be out of pace in every 3D-RX set, this yields large motion artifacts in every reconstruction. Reliability of this system is imposed by the motor controller. In our experiments, two measurements (one from either experiment) with a clear visible deviation are redone.

A. Experiment 1: Number of projection images

In our prototype system the $D_{\text{x ray}}$ is fixed and $f_{\text{x ray}}$ is set to obtain the highest possible number of projection images, which means that the number of projection images available for each reconstruction is inversely proportional to the number of phases [Eq. (2)]. In other words there is a trade-off in our system between the image quality (determined by the number of projections that can be used for reconstruction) and the temporal resolution of the system (the number of phases of object motion that can be obtained). If the number of projection images for a single reconstruction increases, the number of available phases decreases and at the same time the frequency of the object also increases [Eq. (1)].

Preliminary experiments in a static situation showed that using less then 25 projection images yields unacceptable 3D-RX image quality. The upper boundary for the number of images is determined by the object speed which should not exceed 1.5 Hz for clinical reasons. Furthermore, all 3D-RX projection image sets should cover the total propeller angle $\phi_{\text{C-arm,total}}$ of 180 degrees+cone angle (together 196 degrees).

To see the effect of the number of projection images on the contrast resolution and spatial resolution, two object frequencies are used. At these object frequencies, reconstructions of a bullet and rod phantoms (Fig. 3) are generated with the settings from Table I (measurements 1 and 2). The bullet and rod phantom is routinely used to quick check image quality of rotational x-ray systems. As a reference, a high quality measurement 3 is done on the same phantom in a stationary situation. To investigate the severity of the motion artefacts in measurements 1 and 2, measurements 4 and 5 are performed with identical number of input projections but without motion.

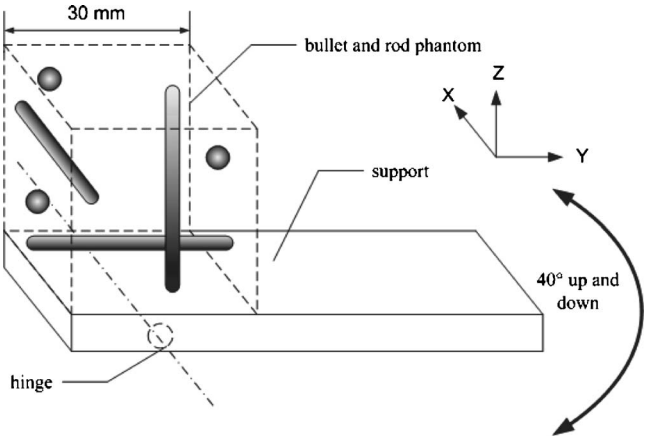

FIG. 3. The position of the bullet and rod phantom on the movement device. The bullet and rod phantom is 3^3 cm^3 Plexiglas cube with three orthogonal metal rods (cylinders with diameter 2 mm and height 30 mm) and three metal bullets with diameter 4 mm.

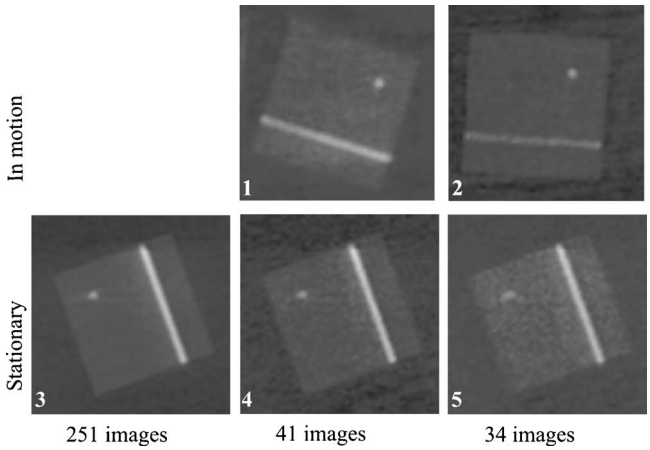

FIG. 4. A single slice (thickness 0.7 mm) of measurement 1–5. These sections are imaged in the *XZ* plane. Two orthogonal rods are imaged in these slices.

The contrast resolution can be characterized by the contrast-to-noise ratio (CNR). A cube of 16^3 voxels is analyzed in a homogenous part of the phantom as well as in air. The standard deviation which was comparable in air and in the phantom material was taken as the noise figure and the mean value difference between air and the phantom as contrast number. The CNR is determined by dividing the noise by the contrast number.

The spatial resolution in terms of the full width at half maximum (FWHM) of the PSF was measured by means of the edge spread function (ESF) as described by Buhr *et al.*[22] A nonisotropic 3D Gaussian was used as a model of the PSF to define a theoretical ESF, which is fit to edges in the image. The FWHM of the PSF was determined on ten edges in all three directions, measuring approximate 25 contours per edge. The streak artifacts sometimes interfered with the ESF determination, therefore ten measurements were done. As described in the former section, one should notice the PSF is expected to be smaller in the direction of motion due to the acquisition geometry and absence of Parker weighting.

From Fig. 4 and Table I it shows that the use of 41 instead of 34 images yields improvement of image quality both for contrast and spatial resolution. The stationary measurements 4 and 5 show minor CNR improvement compared to their similar moving measurements 1 and 2.

In Table I the $\mathrm{PSF}_{\perp\ \mathrm{motion}}$ (the FWHM of the PSF averaged over the *X* and *Y* axis) is shown as well as the $\mathrm{PSF}_{\parallel\ \mathrm{motion}}$ (the FWHM of the PSF parallel with the motion direction, i.e., *Z* axis). The $\mathrm{PSF}_{\perp\ \mathrm{motion}}$ and $\mathrm{PSF}_{\parallel\ \mathrm{motion}}$ FWHM together give a description of the spatial resolution the all measurements should be compared with measurement 3. This shows that deterioration of image quality is mostly due to suboptimal sampling of the projection images when comparing measurements 1 and 2 with their static counterparts' measurements 4 and 5.

Influences of motion artifacts will affect the FWHM of $\mathrm{PSF}_{\parallel\ \mathrm{motion}}$ mostly. The motion blur is most evident in measurement 2 as from the $\mathrm{PSF}_{\parallel\ \mathrm{motion}}$ can be noticed. Measurement 1 does not show significant deviation from its static counterpart measurement 4.

B. Experiment 2: 4D-RX imaging of a post mortem wrist

A postmortem wrist is imaged in 4D-RX to show the obtainable image quality. The wrist is fixed in the movement

TABLE I. Measurement setup and results of image quality evaluation for investigation of the influence of the number of projection images on the reconstruction. In all measurements the $f_{\mathrm{x\ ray}}=12.5$ Hz and $D_{\mathrm{x\ ray}}=30$ s. Note—CNR=contrast-to-noise ratio. PSF=point spread function. SD=standard deviation. ‖motion=Parallel to the motion (in the *Z* direction). ⊥motion=Averaged over the directions orthogonal to the motion (the *X* and *Y* direction).

Measurement	n_{phase} s	f_{object} (Hz)	Pulse length (ms)	$n_{\mathrm{projections}}$	$\phi_{\mathrm{C\text{-}arm,total}}$ (°)	CN R	$\mathrm{PSF}_{\parallel\mathrm{motion}}\pm\mathrm{SD}$ FWHM (mm)	$\mathrm{PSF}_{\perp\mathrm{motion}}\pm\mathrm{SD}$ FWHM (mm)
1	9	1.38	10	41	199	3.0	0.7±0.1	1.5±0.3
2	11	1.13	10	34	201	2.9	1.0±0.2	2.2±0.5
3	1	0	13	251	202	6.9	0.6±0.1	1.1±0.2
4	1	0	13	41	202	4.0	0.6±0.1	1.4±0.2
5	1	0	13	34	202	3.5	0.7±0.1	2.2±0.3

FIG. 5. Three volume renderings of the post mortem wrist of experiment 2. The three images represent three different phases in the joint motion cycle. The viewing angle is located midway between a coronal and a sagittal view. In the volume rendering some parts of the movement device, the support, hinge, and a small metal bullet, are also imaged.

device. Settings are identical to experiment 1, measurement 1. Figure 5 shows three of the nine phase's volume rendered. The same phases are shown in sagittal slices at the height of the lunate in Fig. 6. For both figures the visually optimal window/level settings are used.

Although both volume rendering and slice views show artifacts (Figs. 5 and 6), the anatomical structures of the carpal bones are clearly visible. Most of these streak artifacts and shadowing are due to suboptimal sampling and surrounding structures. The contrast of the bony structures is sufficient not to be influenced significantly by the artifacts. A comprehensible representation of the 3D joints' kinematics is contained in the three different phases of motion that are shown.

V. DISCUSSION

Dynamic imaging of the wrist and other joints for diagnostic purposes may be of great help for assessing functional disorders of the joint. Current imaging systems cannot make dynamic 3D images of the moving wrist. Therefore, we developed a method called 4D-RX, in which a prototype mobile rotational x-ray system is used together with a device suitable for imposing synchronized cyclic movement of the wrist.

The presented method is expected to provide better insight into dynamic motion patterns than 2D video fluoroscopy. Due to the three-dimensional dynamic character and potential for quantitative measurements of 3D motion patterns, by means of segmentation and matching, our method is potentially a valuable support for diagnosis of wrist disorders. State of the art quasidynamic CT imaging of the carpals lacks representation of the true clinically relevant dynamic situation, since hysteresis and acute changes in motion patterns will not be revealed. Our system is able to image a dynamic forced motion pattern of the wrist provided the pattern reproduces over multiple cycles.

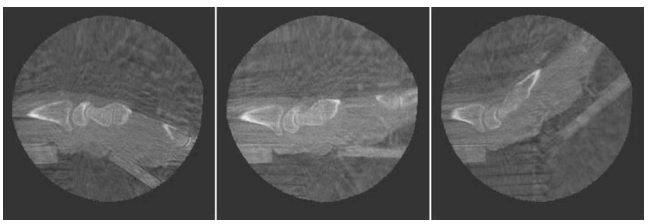

FIG. 6. Three sagittal slices (thickness 0.7 mm) of the postmortem wrist of experiment 2 at the height of the lunate. The phases of the slices correspond to those of the volume renderings of Fig. 5.

The number of input projection images needed for adequate 3D-RX reconstruction quality was examined with a bullet and rod phantom. The image quality was analyzed with the CNR and the PSF. The FWHM of the PSF was determined from the ESF fitted to the image data. The absence of Parker weighting in our reconstruction processes causes anisotropy in the PSF. Both the PSF and CNR show that the 4D-RX image quality is similar to 3D-RX image quality when using 41 images. The main deterioration of these images is due to the low number of projection images and not to the motion of the object. The use of 34 images yields a considerable decrease in image quality, especially in spatial resolution parallel to the direction of the movement. The less image quality obtained with 34 images could also be a synchronization error but this is unlikely when looking at the images of Fig. 4.

In the current system there is a trade-off between the temporal resolution and the reconstruction quality. Using a larger number of input projection images for reconstruction may further improve future image quality. This may be achieved by increasing the duration of the scan and increasing the total number of acquired projections. For clinical use, the object frequency should be limited to provide patient comfort. This can be achieved by either decreasing the acquisition frequency or increasing the number of phases [Eq. (1)]. In both cases, the duration of the scan should be increased to ensure a sufficient number of projections for reconstruction [Eq. (2)].

The choice for the use of this mobile 3D-RX system is its flexibility in number of input projections and movement and its mobility to comply with the experimental setting. The main hardware related disadvantages are the limited duration of the scan (max 30 s) and the eight bit detector. Other 3D C-arm systems, like floor and ceiling mounted C-arms used for interventional radiology, have better hardware but are less flexible in use.

For further validation of the method technical exploration on the validity of the assumption of motion cycle reproducibility is also needed. Moreover, the addition of other clinically relevant motion patterns and clinical compatibility of the method are subjects for further study. Apart from the wrist joint this method can be used in a wide range of joints including elbow and feet, which would only require a small modification of the movement device.

In this paper, we showed the feasibility of imaging 3D dynamic motion patterns of cyclically moving carpal bones in the wrist. Despite the presence of noise and suboptimal sampling, anatomical structures are clearly recognizable in the wrist experiment. We expect that 4D-RX will pave the way to improved assessment of joint disorders by detection of 3D dynamic motion patterns in joints.

[a]Electronic mail: b.carelsen@amc.uva.nl

[1]K. J. Fischer, T. T. Manson, H. J. Pfaeffle, M. M. Tomaino, and S. L.-Y. Woo, "A method for measuring joint kinematics designed for accurate registration of kinematic data to models constructed from CT data," J. Biomech. **34**, 377–383 (2001).

[2]S. Van Sint Jan, P. Salvia, I. Hilal, V. Sholukha, M. Rooze, and G. Clapworthy, "Registration of 6-DOFs electrogoniometry and CT medical imaging for 3D joint modeling," J. Biomech. **34**, 1475–1484 (2002).

[3]R. M. Patterson, C. L. Nicodemus, S. F. Viegas, K. W. Elder, and J. Rosenblatt, "High-speed, three-dimensional kinematic analysis of the normal wrist," J. Hand Surg. [Am] **23**, 446–453 (1998).

[4]T. M. Moojen, J. G. Snel, M. J. Ritt, H. W. Venema, J. M. Kauer, and K. E. Bos, "*In vivo* analysis of carpal kinematics and comparative review of the literature," J. Hand Surg. [Am] **28**, 81–87 (2003).

[5]J. G. Snel, H. W. Venema, T. M. Moojen, M. J. P. F. Ritt, C. A. Grimbergen, and G. J. den Heeten, "Quantitative *in vivo* analysis of the kinematics of carpal bones using a deformable surface model and a 3-D matching technique," Med. Phys. **27**, 2037–2047 (2000).

[6]J. J. Crisco, R. D. McGovern, and S. W. Wolfe, "Noninvasive technique for measuring *in vivo* three-dimensional carpal bone kinematics," J. Orthop. Res. **17**, 96–100 (1999).

[7]M. Maas, P. F. Dijkstra, K. E. Bos, and F. Groenevelt, "Dynamics of the painful wrist—a video—fluoroscopic approach," Proceedings of ECR 1997, A008 (1997).

[8]T. Asano, M. Akagi, K. Tanaka, J. Tamura, and T. Nakamura, "*In vivo* three-dimensional knee kinematics using a bi-planar image-matching technique," Clin. Orthop. Relat. Res. **388**, 157–166 (2001).

[9]B. M. You, P. Siy, W. Anderst, and S. Tashman, "*In vivo* measurement of 3-D skeletal kinematics from sequences of biplane radiographs: Application to knee kinematics," IEEE Trans. Med. Imaging **20**, 514–525 (2001).

[10]M. Grass, R. Koppe, E. Klotz, R. Proksa, M. H. Kuhn, H. Aerts, J. op de Beek, and R. Kemkers, "Three-dimensional reconstruction of high contrast objects using C-arm image intensifier projection data," Comput. Med. Imaging Graph. **23**, 311–321 (1999).

[11]V. Rasche, A. Buecker, M. Grass, R. Koppe, J. op de Beek, R. Bertrams, R. Suurmond, H. Kuehl, and R. W. Guenther, "ECG-gated 3D-rotational coronary angiography (3DRCA)," Proceedings of CARS 2002, pp. 827–831 (2002).

[12]M. Kachelriess and W. A. Kalender, "Electrocardiogram-correlated image reconstruction from subsecond spiral computed tomography scans of the heart," Med. Phys. **25**, 2417–2431 (1998).

[13]K. Nieman, M. Oudkerk, B. J. Rensing, P. van Ooijen, A. Munne, R. J. van Geuns, and P. J. de Feyter, "Coronary angiography with multi-slice computed tomography," Lancet **24**, 357:599–603 (2001).

[14]J. J. Sonke, L. Zijp, and M. van Herk, "Acquisition of 4D tomographic data," Med. Phys. **31**, 1800 (2004).

[15]J. J. Sonke, L. Zijp, P. Remeijer, and M. van Herk, "Respiratory correlated cone beam CT," Med. Phys. **32**, 1176–1186 (2005).

[16]B. Carelsen, N. H. Bakker, S. N. Boon, W. J. Fokkens, N. J. M. Freling, and N. J. Noordhoek, "Mobile 3D rotational x-ray: comparison with CT in sinus surgery," Med. Mundi **48**, 4–10 (2004); www.medical.philips.com

[17]L. A. Feldkamp, L. C. Davis, and J. W. Kress, "Practical cone beam algorithm," J. Opt. Soc. Am. A **1**, 612–619 (1984).

[18]R. Koppe, E. Klotz, J. Op de Beek, and H. Aerts, "3D vessel reconstruction based on rotational Angiography," Proceedings CAR'95 (1995).

[19]R. Koppe, E. Klotz, J. Op de Beek, and H. Aerts, "Digital stereotaxy/stereotactic procedures with C-arm based rotation-angiography," Proceedings CAR'96 (1996).

[20]D. L. Parker, "Optimal short scan convolution reconstruction for fanbeam CT," Med. Phys. **9**, 254–257 (1982).

[21]T. Wu, A. Stewart, M. Stanton, T. McCauley, W. Philips, D. B. Kopans, R. H. More, J. W. Eberhard, B. Opsahl-Ong, L. Niklason, and M. B. Williams, "Tomographic mammography using a limited number of low-dose cone-beam projection images," Med. Phys. **30**, 365–380 (2003).

[22]E. Buhr, S. Gunther-Kohfahl, and U. Neitzel, "Accuracy of a simple method for deriving the presampled modulation transfer function of a digital radiographic system from an edge image," Med. Phys. **30**, 2323–2331 (2003).